

Drivers of Nickel Distribution and Seasonality in the Southern Ocean: New Perspectives From the GEOTRACES G1pr07 Transect



Key Points:

- Higher winter dissolved nickel in the Antarctic Zone surface mixed layer due to decreased biological uptake compared to summer
- Ni is retained in the particle phase longer than phosphorus, which impacts their different depth profiles in the Southern Ocean
- Remineralization of particle-associated nickel is an insignificant source of dissolved nickel compared to the supply from physical mixing

Supporting Information:

Supporting Information may be found in the online version of this article.

Correspondence to:

R. Cloete,
ryan.cloete@univ-brest.fr;
ryan.cloete76@gmail.com





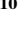




Citation:

Cloete, R., Planquette, H., van Horsten, N. R., Samanta, S., Chen, X.-G., Achterberg, E. P., et al. (2025). Drivers of nickel distribution and seasonality in the Southern Ocean: New perspectives from the GEOTRACES G1pr07 transect. *Journal of Geophysical Research: Oceans*, 130, e2024JC021542. <https://doi.org/10.1029/2024JC021542>

Received 3 JUL 2024
Accepted 14 DEC 2024

Author Contributions:

Conceptualization: R. Cloete, H. Planquette, E. P. Achterberg, R. Middag, S. Fietz, A. N. Roychoudhury
Data curation: R. Cloete, H. Planquette, N. R. van Horsten, E. P. Achterberg, R. Middag, D. J. Janssen, A. R. Bowie, P. van der Merwe, J. C. Looock, T. N. Mtshali, A. N. Roychoudhury
Formal analysis: R. Cloete, H. Planquette, N. R. van Horsten, X.-G. Chen, J. C. Looock
Funding acquisition: H. Planquette, S. Fietz, A. N. Roychoudhury
Investigation: R. Cloete, H. Planquette, S. Samanta, X.-G. Chen, E. P. Achterberg,

R. Cloete^{1,2} , H. Planquette² , N. R. van Horsten^{1,2,3,4}, S. Samanta^{1,5}, X.-G. Chen⁶, E. P. Achterberg⁷ , R. Middag^{8,9} , D. J. Janssen¹⁰ , A. R. Bowie¹¹ , P. van der Merwe¹¹ , J. C. Looock¹, T. N. Mtshali¹² , S. Fietz¹, and A. N. Roychoudhury¹ 

¹Centre for Trace Metal and Experimental Biogeochemistry (TracEx), Department of Earth Sciences, Stellenbosch University, Stellenbosch, South Africa, ²CNRS, University Brest, IRD, Ifremer, Laboratoire des Sciences de l'environnement Marin, Plouzané, France, ³Southern Ocean Carbon - Climate Observatory, CSIR, Cape Town, South Africa, ⁴Now at Department of Physics and Earth Sciences, Constructor University GGmbH, Bremen, Germany, ⁵Now at School of Geoscience, University of the Witwatersrand, Johannesburg, South Africa, ⁶Ocean College, Zhejiang University, Zhoushan, China, ⁷GEOMAR Helmholtz Centre for Ocean Research Kiel, Kiel, Germany, ⁸Department of Ocean Systems (OCS), NIOZ Royal Netherlands Institute for Sea Research, Texel, Netherlands, ⁹CIO-Oceans, Energy and Sustainability Research Institute Groningen, Faculty of Science and Engineering, University of Groningen, Groningen, Netherlands, ¹⁰Eawag—Swiss Federal Institute of Aquatic Sciences and Technology, Department Surface Waters, Kastanienbaum, Switzerland, ¹¹Institute for Marine and Antarctic Studies, University of Tasmania, Battery Point, TAS, Australia, ¹²Department of Forestry, Fisheries and Environment, Oceans and Coast, Cape Town, South Africa

Abstract Winter dissolved nickel (dNi) and particulate nickel (pNi) concentrations were measured in the Southern Ocean (GEOTRACES G1pr07 transect) to investigate biogeochemical cycling within the water column and over seasonal timescales. Concentrations of dNi ranged from 1.98 to 8.21 nmol kg⁻¹ with low surface concentrations and maxima in deepest sampled water masses. Combining our winter data with the GEOTRACES Intermediate Data Product (2021) shows insignificant seasonal dNi variation in surface waters north of the Antarctic Polar Front, indicating the dominance of year-round mixing processes. However, lower summer concentrations than winter in the Antarctic Zone ($\Delta 0.23$ nmol kg⁻¹) suggest a role for biological processes at high latitudes. For pNi, concentrations ranged from 5 to 49 pmol kg⁻¹ with higher values in surface/near-surface water masses. Vertical attenuation factors (*b* values) for pNi (0.19 ± 0.06) and particulate phosphorus (pP; 0.43 ± 0.10) suggest a greater retention of Ni in particles than P, invoking scavenging processes or refractory Ni phases. Water mass analysis shows that remineralization of pNi contributes a maximum of 6% of the highest measured dNi. Instead, dNi distributions and macronutrient relationships were largely explained by phytoplankton uptake in surface waters, and mixing and advection of Atlantic and Antarctic origin water masses, each with different preformed nutrient compositions. Winter trace metal measurements provide new perspectives regarding the balance between biological and physical drivers in the Southern Ocean. For Ni, the biological component is small with respect to physical mixing processes and over the timescales in which water masses accumulate Ni during their transport.

Plain Language Summary Nickel is a nutrient for marine organisms like phytoplankton, which form the base of the marine food web, and are important for globally relevant processes such as carbon cycling. In the ocean, nickel can be dissolved in seawater or associated with particles of diverse compositions. Measuring these nickel forms helps to understand the processes responsible for its distribution throughout the ocean. However, most measurements are from the summer, biasing our understanding toward conditions which favor phytoplankton growth. We therefore measured dissolved and particle-associated nickel in the Southern Ocean during winter to investigate nickel variability over seasonal timescales, and estimate the relative importance of biological and physical processes. Comparing our winter nickel data to existing summer data in the Southern Ocean, we found significantly higher winter concentrations in surface waters at high latitudes (50–60°S), indicating decreased biological utilization of nickel compared to summer. The resupply of Ni from the breakdown of particles was found to be relatively small in comparison to the nickel transported by the water masses making up the Southern Ocean circulation. As a result, physical water mass mixing processes play a more significant role than biological processes in determining nickel distributions in the Southern Ocean.

© 2024. The Author(s).

This is an open access article under the terms of the [Creative Commons Attribution License](https://creativecommons.org/licenses/by/4.0/), which permits use, distribution and reproduction in any medium, provided the original work is properly cited.

R. Middag, D. J. Janssen, A. R. Bowie,
P. van der Merwe, J. C. Looock,
T. N. Mtshali, S. Fietz,
A. N. Roychoudhury
Methodology: R. Cloete, H. Planquette,
N. R. van Horsten, X.-G. Chen,
J. C. Looock, T. N. Mtshali, S. Fietz,
A. N. Roychoudhury
Resources: H. Planquette, T. N. Mtshali,
S. Fietz, A. N. Roychoudhury
Software: R. Cloete, S. Samanta,
X.-G. Chen
Supervision: H. Planquette,
A. N. Roychoudhury
Validation: R. Cloete, J. C. Looock
Visualization: R. Cloete, S. Samanta,
X.-G. Chen
Writing – original draft: R. Cloete
Writing – review & editing:
H. Planquette, N. R. van Horsten,
S. Samanta, X.-G. Chen, E. P. Achterberg,
R. Middag, D. J. Janssen, A. R. Bowie,
P. van der Merwe, J. C. Looock,
T. N. Mtshali, S. Fietz,
A. N. Roychoudhury

1. Introduction

Nickel (Ni) is a trace metal micronutrient present in a number of enzyme systems which are critical for the functioning of microorganisms (Ragsdale, 2009). The most studied Ni-containing enzymes in marine phytoplankton are urease, the Ni isoform of superoxide dismutase (Ni-SOD), and nickel iron (NiFe) hydrogenase (Li et al., 2022; Twining & Baines, 2013). Urease is involved in nitrogen acquisition and fixation, Ni-SOD controls levels of reactive oxygen and nitrogen species thereby limiting potential toxicity and controlling cellular processes related to these molecules, and NiFe hydrogenase helps diazotrophs optimize their metabolic efficiency by reducing energy losses associated with H₂ production during nitrogen fixation. Ni availability may be particularly important for phytoplankton groups such as diatoms who show species-dependent increases in urease activity under nitrate-replete conditions (Peers et al., 2000), such as those found in the Southern Ocean. Like diatoms, phytoplankton groups such as cyanobacteria may have additional Ni requirements due to the presence of Ni-SOD. In open-ocean diatoms, multiple SOD isoforms are expressed (Cuvelier et al., 2010). In particular, Ni-SOD may have evolved as a mechanism to reduce iron (Fe) quotas related to Fe-SODs in the modern ocean (Dupont, Neupane, et al., 2008). For cyanobacteria, Ni-SOD is found in all strains of *Prochlorococcus* and in most strains of *Synechococcus* (Dupont, Barbeau, & Palenik, 2008; Dupont, Neupane, et al., 2008) which supports the high cellular Ni content relative to other eukaryotic phytoplankton groups such as flagellates (Twining et al., 2012). Despite the requirement of Ni by phytoplankton, surface ocean Ni concentrations are never fully depleted (>1.5 nmol kg⁻¹). Hypotheses for the persistence of moderate surface Ni concentrations include the presence of poorly bioavailable Ni or a low biological demand relative to other (macro)nutrients (Archer et al., 2020; John et al., 2022, 2024; Lemaitre et al., 2022; Middag et al., 2020; Yang et al., 2021).

Phytoplankton assimilate dissolved (<0.2- μ m pore-size-filtered seawater) Ni (dNi) in the surface euphotic zone and produce particulate (>0.45- μ m pore size filter) biogenic Ni (pNi). Subsequent processes such as zooplankton grazing and adsorption onto particles (including particles of lithogenic and authigenic composition), result in the formation of larger particles which may influence the vertical export of Ni and other nutrients (Lam & Marchal, 2015). Sinking particles may also undergo disaggregation via remineralization, desorption, and dissolution which may in turn contribute a recycled source of dNi to the water column. These internal cycling processes manifest as surface depletions in dNi and enrichments in pNi (i.e., nutrient-type distributions). However, their distributions are not necessarily mirror images of each other considering that biological and physical processes lead to differences in their residence times, with thousands of years for dissolved Ni phases (Sclater et al., 1976) compared with days to months for particulate Ni phases (Lam & Marchal, 2015). In oceanic distributions, these vertically driven processes are superimposed on large-scale ocean circulation. Basin scale mixing and advection of water masses with various origins and preformed end-member compositions play a major role in transporting dNi (Chen et al., 2024; Janssen et al., 2020; Middag et al., 2020) and other micro/macronutrients (De Souza & Morrison, 2024; Sarmiento et al., 2004; Vance et al., 2017) globally and maintaining concentration gradients and stoichiometric relationships with macronutrients. Furthermore, dynamic seasonal mixing processes with enhanced deep winter mixing may contribute to surface dNi (and other trace metals) variability on shorter timescales, particularly in the Southern Ocean (Cloete et al., 2019; Tagliabue et al., 2014).

The increase in trace metal data availability, particularly since the start of the GEOTRACES program (Anderson, 2020), has improved our knowledge of Ni cycling in the ocean. Yet spatial and seasonal gaps in the global Ni database exist, particularly in the Indian sector of the Southern Ocean. For logistical reasons, existing measurements in the Southern Ocean are heavily skewed toward spring/summer seasons when conditions are favorable for phytoplankton growth (e.g., increased light levels and shallow, more stable mixed layers). The winter months may be critical for resupply of Ni (Cloete et al., 2019; Ellwood, 2008) and other micronutrients such as Fe (Tagliabue et al., 2014) from subsurface to surface waters thereby sustaining phytoplankton growth over the subsequent spring and summer seasons. In this context, this study aims to improve our understanding of the drivers of biogeochemical cycling of Ni in the ocean by contributing the first wintertime dissolved and particulate Ni measurements from the western Indian sector (GEOTRACES meridional section GIpr07) of the Southern Ocean.

2. Methods

2.1. Sample Collection

Seawater samples were collected onboard the RV SA *Agulhas II* during a 2017 austral winter cruise (28/06/2017–13/07/2017) occupying the GEOTRACES GIpr07 transect in the Indian sector of the Southern Ocean (Figure 1).

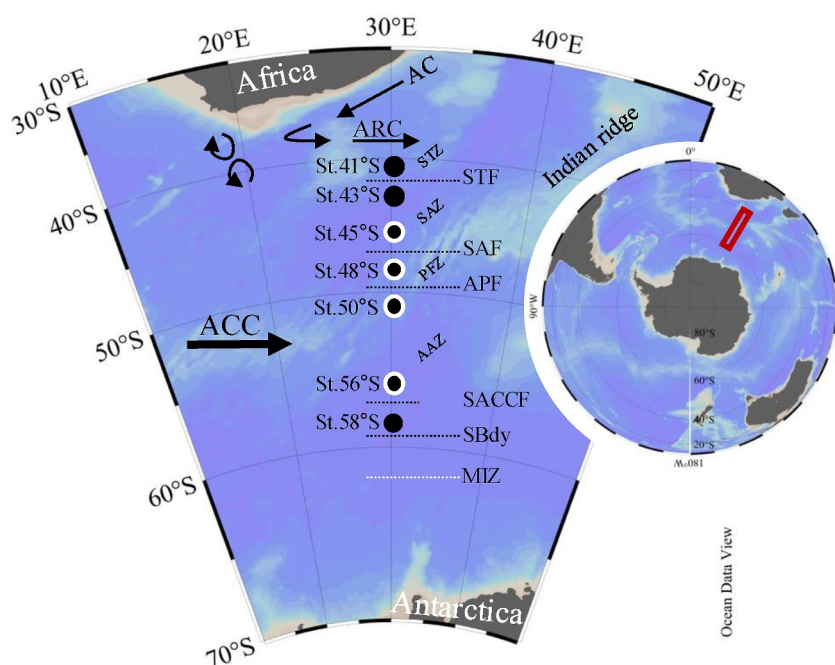


Figure 1. Station locations during the 2017 Winter Cruise along the GEOTRACES G1pr07 transect (30°E longitude). Black circles are shallow stations (1,500 m), and white borders are deep stations (up to 4,250 m). Positions of the frontal systems intersected and corresponding oceanic zones as well as the main surface currents are shown. Acronyms in alphabetical order are as follows; AAZ: Antarctic Zone; AC: Agulhas Current; ACC: Antarctic Circumpolar Current; APF: Antarctic Polar Front; ARC: Agulhas Return Current; MIZ: marginal ice zone; SACCF: Southern Antarctic Circumpolar Current Front; SAF: Subantarctic Front; SAZ: subantarctic Zone; SBdy: Southern Boundary; STF: subtropical front; and STZ: subtropical zone. Figure constructed using Ocean Data View (Schlitzer, 2023).

Seven stations, including four deep (up to 4,250 m) and three shallow (less than 1,500 m), were sampled between 41 and 58°S allowing observations across important frontal systems and in different water masses. Samples were collected using 24 internally Teflon-coated polyvinyl chloride (PVC) 12-L GO-FLO sampling bottles (General Oceanics) mounted on a GEOTRACES compliant rosette frame (Cutter et al., 2017) which also housed a Seabird 9+ CTD (conductivity, temperature, and depth) recorder. Discrete samples for salinity (S) and dissolved oxygen (O_2) were collected and analyzed onboard for the calibration of CTD sensor measurements of conductivity (8410A Portasal salinometer) and oxygen (Metrohm 848 Titrino plus). Temperature and salinity measurements were used to calculate potential density (σ_θ) in order to characterize sampled water masses and calculate the mixed layer depth (MLD) (Cloete et al., 2021). The GO-FLO bottles were triggered at predetermined depths during the upcast. Directly upon recovery of the rosette, the GO-FLO bottles were transported into a class 100 clean container lab for subsampling. Samples for dissolved trace metal determination were collected in duplicates in 125-mL acid-cleaned low-density polyethylene (LDPE, Nalgene) bottles after online filtration through 0.2- μ m Sartobran membrane filter capsules (Sartorius) and under pure nitrogen pressure (N_2 , 0.5 bar, Air Products). After filtration and under a laminar flow hood, samples were acidified to 0.024 M hydrochloric acid (HCl Ultrapur® 30%, Merck), resulting in a pH of \sim 1.7, and stored at room temperature for later analysis. Thereafter, precleaned filters (25 mm diameter and 0.45 μ m pore size, Supor) were mounted on acid-washed Swinnex (Millipore) filter holders and attached to the GO-FLO spigots (Planquette & Sherrell, 2012). The remaining volume in each GO-FLO bottle was filtered for particulate trace metal determination. Filtrate was collected in buckets from which the filtered volume was measured (between 5 and 10 L). After filtration, filter holders were removed and disassembled before the sampled filter was transferred to an acid-washed polystyrene Petri dish using clean plastic forceps. Collected filters were subsequently frozen at -20°C for transport back to land. Handling of all filters, filter holders, and samples was done under a laminar flow hood.

Macronutrient (nitrate (NO_3), nitrite (NO_2), silicic acid ($\text{Si}(\text{OH})_4$), and phosphate (PO_4)) samples were collected from GO-FLO bottles in 50-mL Falcon tubes, filtered (0.2 μ m) immediately after collection and stored frozen at -20°C until analysis (<3 months).

Table 1
Results for dNi and pNi From the Analysis of Various Reference Materials

	dNi (nmol kg ⁻¹)		pNi (nmol kg ⁻¹)
GSC 1-19		PACS 3	
Consensus	4.39 ± 0.21	Certified	0.68 ± 0.05
Measured (n = 5)	3.93 ± 0.14	Measured (n = 5)	0.68 ± 0.01
GSP-62		MESS 4	
Consensus	2.60 ± 0.10	Certified	0.73 ± 0.03
Measured (n = 5)	2.44 ± 0.12	Measured (n = 5)	0.84 ± 0.04
NASS-7		BCR 414	
Certified	4.14 ± 0.31	Certified	0.32 ± 0.01
Measured (n = 5)	3.85 ± 0.10	Measured (n = 5)	0.31 ± 0.04
Blank (n = 5)	0.033 ± 0.004	Filter Blank (n = 5) (pmol kg ⁻¹ filter ⁻¹)	7 ± 1
Limit of Detection (n = 5)	0.011	Limit of Detection (n = 5) (pmol kg ⁻¹)	4

Note. Consensus dNi values for GSC and GSP as of 2019. Certified values for NASS-7 as of 2018. For pNi, PACS 3-, MESS 4-, and BCR 414-certified values from 2015, 2015, and 2017, respectively. Blank and filter blank values as well as ICP-MS limit of detection (calculated as 3 times the standard deviation of the blank/filter blank) are also shown.

2.2. Dissolved Nickel (dNi) and Macronutrient Determination

Seawater samples for dissolved metal analysis were processed at Stellenbosch University (SUN, South Africa) according to established methods (Samanta et al., 2021). Briefly, samples were preconcentrated 40-fold using a SC-4 DX seaFAST module (Elemental Scientific Inc). Thereafter, a suite of trace metals including dNi, were measured in duplicates via a single quadrupole inductively coupled plasma mass spectrometer (Q-ICPMS). The accuracy of the measurements was verified by analysis of NASS-7-certified reference seawater and GEOTRACES GSC and GSP community reference seawater (Table 1). Procedural blanks for Ni were 0.033 ± 0.004 nmol kg⁻¹ and the limit of detection (LOD), calculated as three times the standard deviation of the procedural blank, was 0.011 nmol kg⁻¹ (Table 1).

Concentrations of NO₃ + NO₂ and Si(OH)₄ were analyzed using a Lachat Quick-Chem flow injection analyzer. NO₂ and PO₄ concentrations were determined manually by a colorimetric method. The concentration of NO₃ was calculated by subtraction ([NO₃ + NO₂] - [NO₂]). All analyses were conducted at the Marine Biogeochemistry laboratory at the University of Cape Town (MBL-UCT) with further details reported in Weir et al. (2020).

2.3. Particulate Nickel (pNi) and Phosphorous (pP) Determination

Samples for particulate trace metals were analyzed at Pôle Spectrométrie Océans (PSO, Plouzané, France) and were processed and analyzed 6 months after sample collection. Details of the analytical procedure (Planquette & Sherrell, 2012) are presented briefly here. Filters were acid reflux-digested at 130°C for 4 hr in acid-cleaned Savillex vials with a 6-M HNO₃/1.4 M HF solution (Ultrapur[®], Merck) and allowed to cool before being evaporated to near dryness. Then, 400 μL of concentrated HNO₃ (Ultrapur[®], Merck) was added to drive off the fluorides before a second evaporation procedure. Archive solutions were stored in 3 mL of 0.12 M HNO₃ (Ultrapur[®]; Merck), of which 250 μL was diluted up to 2 mL for analysis by sector field inductively coupled plasma mass spectrometry (SF-ICP-MS, Element XR Thermo Scientific). Samples were spiked with 1 μg L⁻¹ indium (In) as an internal standard to correct for instrument drift. Three certified reference materials (PACS 3, MESS 4, and BCR 414) were processed as samples and analyzed for pNi to assess the accuracy of the methodology (Table 1). The certified reference materials (PACS 3, MESS 4, and BCR 414) yielded mean percentage recoveries of 100 ± 1%, 115 ± 5%, and 98 ± 13% for pNi, respectively. Filter blanks for pNi (7 ± 1 pmol kg⁻¹ per filter) were determined by digesting and analyzing unused acid-washed filters (n = 5). Final pNi values represent blank subtracted concentrations. The limit of detection for pNi, defined as three times the standard deviation of the filter blanks, was 4 pmol kg⁻¹ (Table 1). Results for pP have been previously published (Cloete et al., 2021).

2.4. Water Mass Analysis

An optimum multiparameter (OMP) analysis was performed to calculate the percentage contributions of important subsurface water masses for each sample location (Karstensen & Tomczak, 1998; Tomczak & Large, 1989) (Figure S1 in Supporting Information S1). The focus of the OMP was on subsurface water masses; therefore, samples with depths <200 m and/or temperature >10°C were excluded from the analysis to avoid the influence of surface biological processes on nutrient concentrations. Six water masses were considered, namely Subantarctic Surface Water (SASW), Antarctic Intermediate Water (AAIW), North Atlantic Deep Water (NADW), Upper Circumpolar Deep Water (UCDW), Lower Circumpolar Deep Water (LCDW), and Antarctic bottom water (AABW). End-member characteristics for temperature, salinity, oxygen, phosphate, nitrate and silicic acid (Table S1 in Supporting Information S1) were defined by considering the property-property plots of the data from this section (Figure S2 in Supporting Information S1) as well as the end-member values given by Chen et al. (2024). The end-member values compared reasonably well with those defined in previous Southern Ocean OMP analyses (Table S1 in Supporting Information S1), with variances attributable to differences in regional Southern Ocean hydrography. A linear fit regression model was used to predict the end-member dNi concentrations of water masses (program R version 4.3.1), and then reconstruct the dNi concentrations by direct multiplication of water mass fractions with their end-member compositions. Therefore, our methodology can be used to assess whether the dNi distributions can be reconstructed by water mass mixing without invoking other processes. Residual concentrations (calculated as the difference between measured and predicted values) for dNi (and other parameters) (Figure S3 in Supporting Information S1) therefore suggest external sources (positive residuals) or sinks (negative residuals), respectively. Similarly, the O₂ deficit was calculated as the difference between measured and predicted O₂ concentrations and used to estimate the amount of remineralization that occurred relative to the end-member composition based on a Redfield ratio of $\Delta P:\Delta N:\Delta Si:\Delta O_2 = 1:16:40:170$ (Anderson & Sarmiento, 1994; Karstensen & Tomczak, 1998). Assuming the O₂ deficits are solely attributed to remineralization of sinking phytoplankton cells, we estimated the amount of remineralized dNi by extending the Redfield ratio to include Ni ($\Delta P:\Delta Ni = (P_1)_{1000}Ni_{1.4}$) based on an upper estimate of phytoplankton cellular pNi: pP quotas (1.4 mmol mol⁻¹ (Twining & Baines, 2013);).

The uncertainties of water mass contributions in the OMP analysis (Figure S3 in Supporting Information S1) were estimated by summing the residuals of temperature, salinity, oxygen, and nutrients scaled by their weights, as per Evans et al. (2020). The generally higher water mass uncertainties (>0.1) at depth are likely from lower depth resolution of samples in LCDW and AABW. For this reason, we combine their fractional contributions (LCDW + AABW; Figure S1 in Supporting Information S1).

2.5. Seasonal Compilation of Existing Measurements

In order to investigate potential seasonal variations in dNi, we compared our median MLD concentrations (median \pm sd) to a compilation of median MLD concentrations covering all three Southern Ocean sectors (Atlantic, Indian, and Pacific) over multiple seasons. For pNi, to avoid biases related to the variable vertical distribution of biomass, we identified the depth of the chlorophyll maximum (Chl_{max}) in the mixed layer at each sampling location and took the median of pNi concentrations (median \pm sd) from the depth range corresponding to $100 \pm 30\%$ Chl_{max} . Data from June through August were considered as ‘winter’ while November through March were considered as ‘summer’ as the majority (>90%) of these measurements were taken between December and February. The Wilcoxon-Mann-Whitney test (confidence interval of 95%) was performed to assess whether or not seasonal differences in measured parameters were significant. The comparative data were primarily derived from the GEOTRACES Intermediate Data Product (GEOTRACES Intermediate Data Product Group, 2021) but also included data published outside of the IDP2021 (see Table 2 for data references and Figure S4 in Supporting Information S1 for compilation metadata). The compilation also includes pNi and pP data from GEOTRACES transects GS01 and GIpr05 which are previously unpublished (see Table S2 in Supporting Information S1 for data validation). See Traill et al. (2024) and van der Merwe et al. (2019) for further information regarding particulate trace element analysis and transect hydrography.

2.6. Calculation of Vertical Attenuation Factors (*b* Values)

The remineralization length scale of an element is determined by the attenuation of the downward particle flux settling gravitationally and is element-specific (Boyd et al., 2017). The attenuation of Ni with depth was modeled

Table 2
Data References for the Southern Ocean Ni Compilation

Section/cruise	Reference
GA02	(Middag et al., 2020)
GA10	(Archer et al., 2020; Chen et al., 2024)
GIPr05	Bowie, Holmes, Schallenberg, and van der Merwe, Wuttig, unpublished
GIPr07	This study
GIPY01	Ellwood, unpublished
GIPY06	Bowie, Butler, Lannuzel, O'Sullivan, Remenyi, and Watson, unpublished
GP19	Minami, Sohrin, and Zheng, unpublished
GS01	Bowie, Holmes, Gault-Ringold, Latour, van der Merwe, and Wuttig, unpublished
GSc01	(Janssen et al., 2020)
CROZEX	(Castrillejo et al., 2013)
IN2016_V02	(Ellwood et al., 2020)
SOLACE	(Grun et al., 2023)
SOSCEX	(Cloete et al., 2019)

Note. Section names according to GEOTRACES Intermediate Data Product (GEOTRACES Intermediate Data Product Group, 2021). Cruise names are given for process studies.

using the Martin equation (Martin et al., 1987), originally developed for particulate organic carbon, modified for trace metals accordingly (Equation 1 (Ellwood et al., 2020)).

$$[pNi_z] = [pNi_{MLD}](z/MLD)^{-b} \quad (1)$$

Here $[pNi_z]$ is the particulate trace metal concentration at depth z , $[pNi_{MLD}]$ is the particulate trace metal concentration nearest the base of the MLD at each station, and b is the vertical attenuation factor. Model fits of the particulate data were optimized by utilizing the least squares method between observational data and the model output.

3. Results

3.1. Hydrography of the Study Area

Physical and biogeochemical properties (macronutrients, salinity, temperature, Chlorophyll-*a*, apparent oxygen utilization, and oxygen) and MLDs have been previously described in detail (Cloete et al., 2021; Van Horsten et al., 2022; Weir et al., 2020). Frontal positions and water masses were determined following temperature, salinity, and oxygen criteria outlined in the literature (Orsi et al., 1995; Pollard et al., 2002; Swart et al., 2010; Talley, 2011). The Southern Ocean is dominated by the eastward flowing Antarctic Circumpolar Current (ACC) (Figure 1). Frontal systems run in parallel with the ACC and separate the Southern Ocean into distinct biogeochemical zones. From north to south, the subtropical front (STF; 42.4°S) defines the boundary between the subtropical zone (STZ) and the subantarctic zone (SAZ). The Subantarctic Front (SAF; 46.2°S) separates the SAZ from the Polar Frontal Zone (PFZ) which extends southward until the Antarctic Polar Front (APF; 49.3°S). Further south, the Antarctic Zone (AAZ) continues until the Southern Boundary (Sbdy; 58.5°S) and includes the Southern Antarctic Circumpolar Current Front (SACCF).

Numerous water masses were sampled along the transect (Figure 2a). From north to south, sampled surface waters comprised subtropical surface water (STSW; ~18°C) and progressively cooler Subantarctic Surface Water (SASW; 5–11°C) and Antarctic Surface Water (AASW; –0.1–1.8°C). In the STZ, South Indian Central Water (SICW; 16–18°C; 100–300 m depth) and Sub-Antarctic Mode Water (SAMW; 12–15°C; 300–500 m depth) were sampled. Antarctic Intermediate Water (AAIW; 26.90–27.45 kg m⁻³; 250–1,000 m depth) was primarily observed subducting northward from the PFZ. Salty, southward flowing North Atlantic Deep Water (NADW; 34.7–34.8 PSU; 1,000–2750 m depth) was most identifiable in the SAZ. The NADW was diluted by mixing with

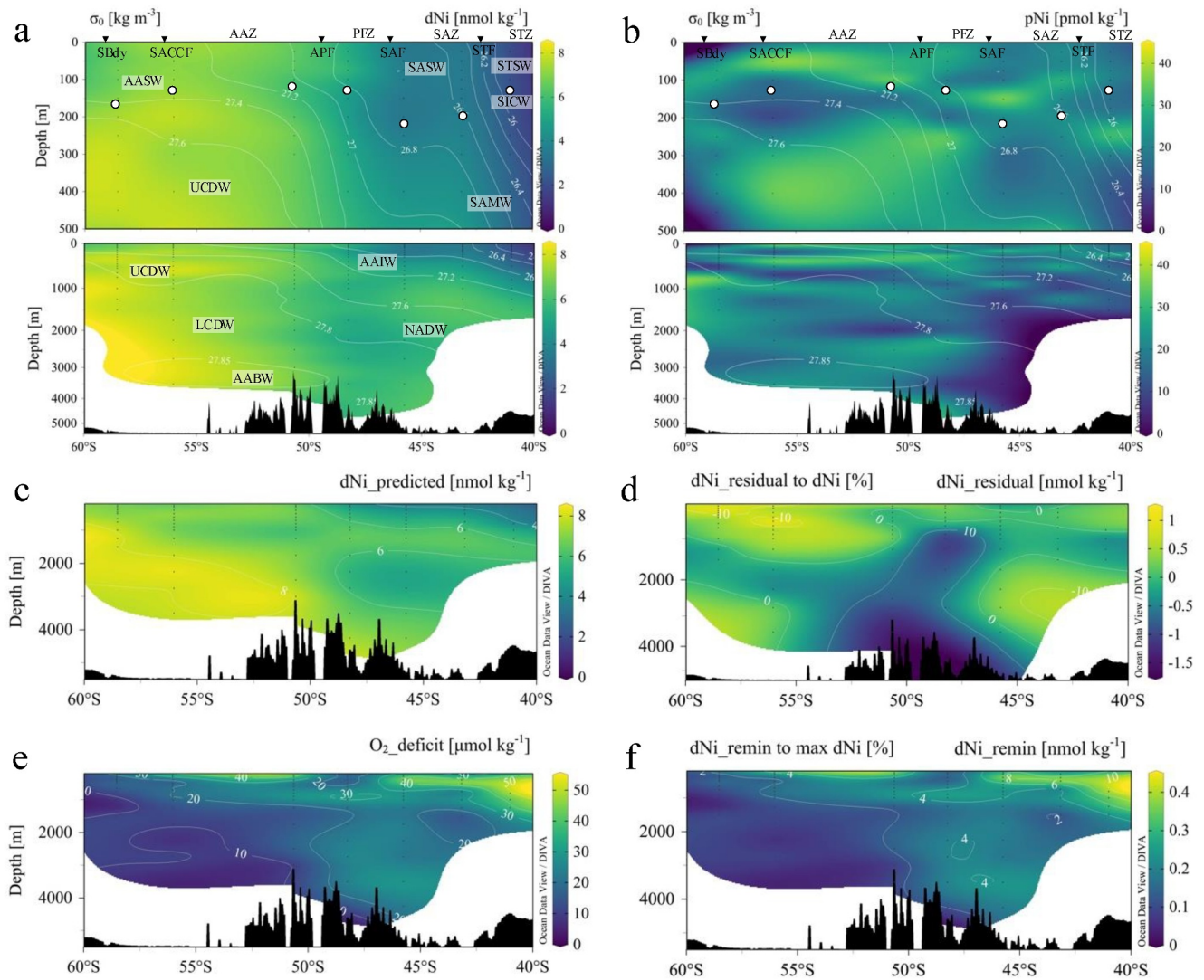


Figure 2. Section plots of (a) dNi overlain with potential density isolines (σ_0), (b) pNi overlain with potential density isolines, (c) dNi predicted from the OMP analysis, (d) residual dNi (difference between measured and predicted dNi) overlain with isolines of the percentage of residual dNi to measured dNi, (e) dissolved oxygen (O_2) deficit (difference between measured and predicted O_2), and (f) remineralized dNi overlain with isolines of the percentage of remineralized dNi to the maximum measured dNi of the transect. Plots (a) and (b) are separated into an upper panel, showing the upper 500 m of the water column, and a lower panel showing the full water column. Note the depth axis of the lower panels is stretched toward the upper water column. Positions of the frontal systems and corresponding oceanic zones are shown along the top of the plots. White dots indicate MLDs. Water masses in alphabetical order are as follows; AABW: Antarctic bottom water; AAIW: Antarctic Intermediate Water; AASW: Antarctic Surface Water; LCDW: Lower Circumpolar Deep Water; NADW: North Atlantic Deep Water; SAMW: Sub-Antarctic Mode Water; SASW: Subantarctic Surface Water; SICW: South Indian Central Water; STSW: subtropical surface water; and UCDW: Upper Circumpolar Deep Water. Figure constructed using Ocean Data View (Schlitzer, 2023).

northward flowing Upper Circumpolar Deep Water (UCDW $27.32\text{--}27.77\text{ kg m}^{-3}$; 200–1,750 m depth) and Lower Circumpolar Deep Water (LCDW; $27.76\text{--}27.85\text{ kg m}^{-3}$; 700–3,500 m depth). Bottom waters were composed of a mixture between LCDW and Antarctic bottom water (AABW; $0.1\text{--}1.3^\circ\text{C}$; $27.82\text{--}27.86\text{ kg m}^{-3}$).

3.2. Vertical Profiles From Section G1pr07

3.2.1. dNi

Along the transect, winter dNi concentrations ranged from 1.98 to 8.21 nmol kg^{-1} (Figure 2a; Table S3 in Supporting Information S1). Vertical profiles of dNi concentrations generally increased with depth; however, the concentration gradient with depth ($\partial\text{Ni}/\partial z$) decreased southward. For example, the ratio of deep (using 1,500 m for all stations) to surface (~ 25 m) concentrations was higher north of the APF (1.8–3.0) than the south (1.0–1.2).

At St. 41°S (STZ), dNi was $2.09 \pm 0.09 \text{ nmol kg}^{-1}$ ($n = 6$) in STSW, increased slightly with depth in underlying SICW ($2.30 \pm 0.04 \text{ nmol kg}^{-1}$; $n = 3$) and SAMW ($2.79 \pm 0.17 \text{ nmol kg}^{-1}$; $n = 3$) before increasing more rapidly in AAIW ($4.52 \pm 0.29 \text{ nmol kg}^{-1}$; $n = 3$) and UCDW ($5.76 \pm 0.22 \text{ nmol kg}^{-1}$; $n = 2$). At the two SAZ stations (St. 43 and 45°S), dNi profiles were very similar. Concentrations in SASW were 3.80 ± 0.36 ($n = 12$) and 3.67 ± 0.31 ($n = 9$) nmol kg^{-1} , respectively, increasing to 6.21 ± 0.17 ($n = 3$) and 5.79 ± 0.24 ($n = 5$) nmol kg^{-1} in UCDW. In the PFZ and AAZ, depth dNi gradients were weaker and showed subsurface variations. For example, at St. 48°S, dNi had a subsurface maximum at 75 m ($5.81 \pm 0.02 \text{ nmol kg}^{-1}$; mean \pm sd of duplicate measurements) and subsurface minimum at 200 m ($4.72 \pm 0.01 \text{ nmol kg}^{-1}$), while at St. 50°S a subsurface minimum at 100 m ($5.98 \pm 0.05 \text{ nmol kg}^{-1}$) and a subsurface maximum at 250 m ($6.92 \pm 0.00 \text{ nmol kg}^{-1}$) were observed. Concentrations of dNi in NADW were lower than overlying UCDW and underlying LCDW and AABW such that a local dNi minima was observed. For example, at St. 45°S, dNi was $5.43 \pm 0.06 \text{ nmol kg}^{-1}$ ($n = 2$) in NADW, $5.79 \pm 0.24 \text{ nmol kg}^{-1}$ ($n = 5$) in overlying UCDW, and $6.12 \pm 0.08 \text{ nmol kg}^{-1}$ ($n = 2$) in underlying LCDW + AABW, respectively (Table S4 in Supporting Information S1).

3.2.2. pNi

Concentrations of winter pNi ranged from 5 to 49 pmol kg^{-1} (Figure 2b; Table S3 in Supporting Information S1). The composition was dominated by non-lithogenic pNi phases (particularly biogenic phases) which contributed >85% of the total pNi pool and $99 \pm 1\%$ in the mixed layer (See Figure S5 in Supporting Information S1). Lowest concentrations were measured in intermediate and deep waters at St. 45°S where pNi was $<7 \text{ pmol kg}^{-1}$ below 1,000 m (Table S4 in Supporting Information S1). For surface water masses, there was no consistent latitudinal trend for pNi; however, concentrations were generally lower in STSW ($18 \pm 1 \text{ pmol kg}^{-1}$; $n = 5$) at St. 41°S and higher in AASW ($26 \pm 13 \text{ pmol kg}^{-1}$; $n = 15$) to the south. Intermediate and deep water masses at St. 50 and 56°S generally had higher pNi concentrations than other stations. For example, pNi in AAIW reached a maximum of $31 \pm 1 \text{ pmol kg}^{-1}$ ($n = 2$) at St. 50°S and decreased to $14 \pm 1 \text{ pmol kg}^{-1}$ ($n = 2$) in AAIW at St. 41°S. For UCDW, a maximum pNi of $28 \pm 7 \text{ pmol kg}^{-1}$ ($n = 3$) was measured at St. 56°S (AAZ) and a minimum pNi of $12 \pm 1 \text{ pmol kg}^{-1}$ ($n = 2$) at St. 41°S (STZ). Within the MLD, pNi displayed variable depth trends with local maxima either near the surface (e.g., St. 48°S and 56°S), near the base of the ML (e.g., St. 50 and 58°S), or in between the surface and MLD (e.g., St. 43°S and 45°S). Surface water maxima for pNi were deeper than pP maxima at most stations (St. 41°S, 48°S, 50°S, and 56°S), pNi and pP maxima were colocated at SAZ stations (St. 43°S and 45°S), and the pNi maximum was shallower than the pP maximum at St. 58°S.

3.3. Predicted dNi From OMP

Predicted dNi distributions (Figure 2c) showed similar concentration ranges and distribution patterns to measured dNi, as indicated by the strong linear correlation between the two; predicted dNi = 0.99 ± 0.10 [measured dNi] ($r^2 = 0.993$; $n = 79$; root mean square error = $0.08 \text{ nmol kg}^{-1}$). As a result, residual dNi concentrations (Figure 2d) were mostly between -0.5 – 0.5 nmol kg^{-1} ($0.01 \pm 0.37 \text{ nmol kg}^{-1}$, mean \pm sd) and <10% of the measured values. The O_2 deficits were always positive (1 – $50 \text{ } \mu\text{mol kg}^{-1}$) meaning predicted O_2 was always greater than measured values (Figure 2e). The O_2 deficits translated to an estimated remineralized dNi component of 0.04 – $0.41 \text{ nmol kg}^{-1}$ ($0.20 \pm 0.08 \text{ nmol kg}^{-1}$, mean \pm sd), representing 1%–10% of measured dNi (Figure 2f) and water mass values of AAIW ($0.23 \pm 0.07 \text{ nmol kg}^{-1}$), UCDW ($0.22 \pm 0.06 \text{ nmol kg}^{-1}$), NADW ($0.19 \pm 0.01 \text{ nmol kg}^{-1}$), and LCDW + AABW ($0.13 \pm 0.06 \text{ nmol kg}^{-1}$).

3.4. Southern Ocean Compilation

Considering all data from the Southern Ocean mixed layer (Figure S4 in Supporting Information S1), dNi showed a minimum concentration of $2.04 \pm 0.06 \text{ nmol kg}^{-1}$ in the STZ and a maximum $7.20 \pm 0.10 \text{ nmol kg}^{-1}$ in the AAZ (both from the GIpr07 section). Median concentrations in the mixed layer increased southward, regardless of the Southern Ocean sector or season (Figure 3a). Comparing seasonal dNi data per zone showed no significant ($p > 0.05$) differences in the STZ, SAZ, or PFZ (Table 3). In contrast, winter dNi in the AAZ ($6.50 \pm 0.44 \text{ nmol kg}^{-1}$; $n = 18$) was significantly ($p < 0.05$) higher than summer values ($6.27 \pm 0.49 \text{ nmol kg}^{-1}$; $n = 97$) (Table 3).

Southern Ocean pNi data are scarce with comparable summer measurements from a zonal section in the subtropical Atlantic ocean (GEOTRACES GA10 transect) and three Southern Ocean data sets, a process study

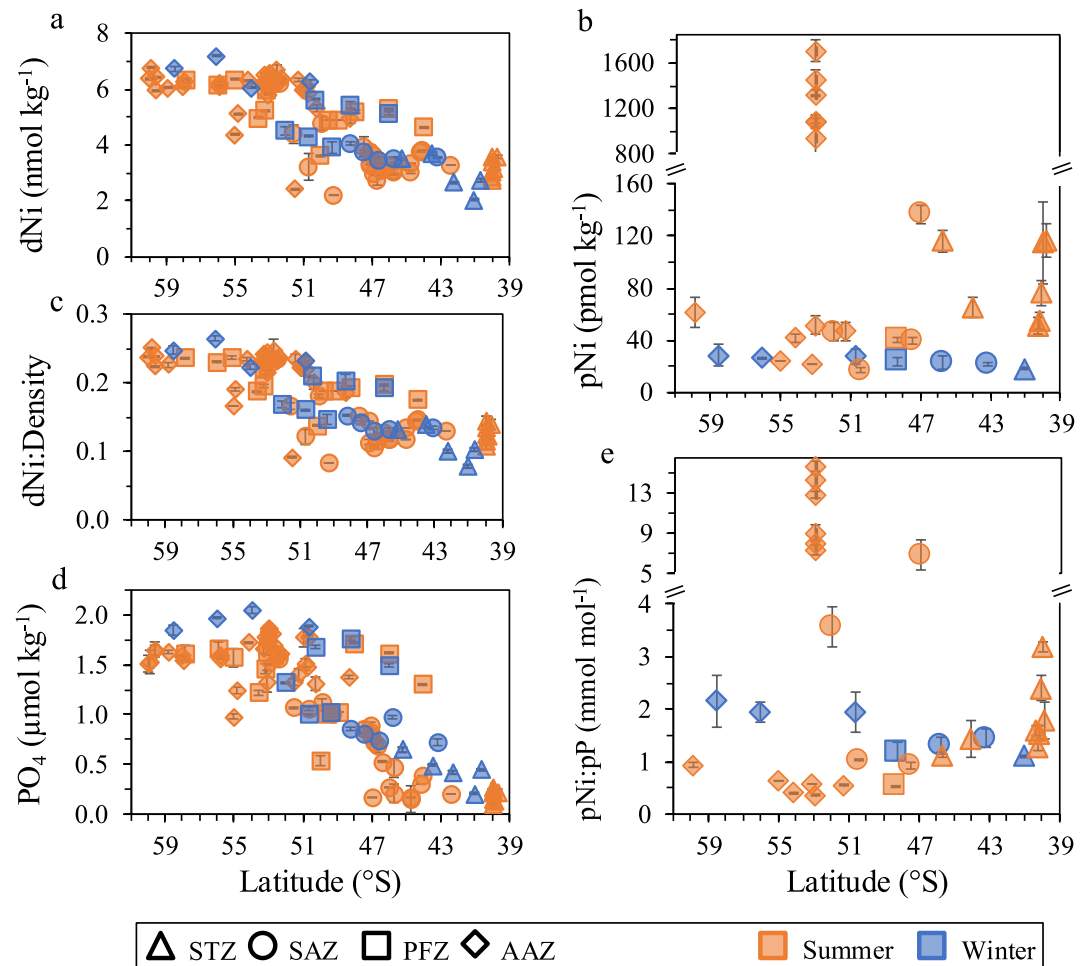


Figure 3. Distribution plots of (a) dNi, (b) pNi, (c) ratios of dNi to seawater density, (d) PO₄, and (e) ratios of pNi to pP, for a compilation of winter (blue) and summer (orange) measurements from the Southern Ocean (see Section 2.5 and Figure S4 in Supporting Information S1 for data compilation details). For a, c, and d, values represent median \pm sd from the surface mixed layer. For b and e, values represent median \pm sd from the depth range corresponding to 100 \pm 30% Chlmax. See Table 2 for a full list of data set references.

around Heard and McDonald Islands (GEOTRACES GIPr05 study), a meridional section south of Australia (GEOTRACES GS01 transect) and three SAZ stations south of Australia (IN2016_V02 expedition) (Figure 3b, Figure S4 in Supporting Information S1). Our winter values from the STZ (18 ± 2 pmol kg⁻¹) were approximately 6-fold lower than summer values from the Atlantic sector (107 ± 70 pmol kg⁻¹) (Table 3). In the SAZ, PFZ and AAZ winter pNi were 23 ± 7 , 24 ± 2 and 30 ± 11 pmol kg⁻¹, respectively, and were also lower ($p < 0.05$) than summer values of 60 ± 47 , 40 ± 4 and 42 ± 26 pmol kg⁻¹, respectively.

4. Discussion

4.1. Physical and Biological Drivers of Surface Water Ni Seasonal Variability

Concentrations of dNi and ratios of dNi to seawater density (dNi:density) showed no significant seasonal differences in the STZ, SAZ, and PFZ (Figures 3c and Table 3). In the AAZ, however, winter dNi concentrations as well as dNi:density ratios were significantly ($p < 0.05$) higher than the summer concentrations. These observations suggest a balance between biological uptake and physical mixing processes in determining the spatial and seasonal variations in surface dNi. At higher latitudes (i.e., the AAZ), seasonal uptake variability appears to have a greater influence on surface dNi, likely because decreased sunlight hours, lower incident light, and deeper mixed layers (winter: 112 ± 22 m vs. summer: 57 ± 26 m for the AAZ stations) in winter create unfavorable physical growth conditions for phytoplankton, resulting in decreased nutrient uptake and hence higher surface nutrient

Table 3
Mixed Layer Median \pm sd Values for dNi, PO₄, Ratios of dNi to Seawater Density (dNi: density), and pNi and pP in the Southern Ocean (Excluding Island-Influenced Data), Grouped by Season and Zone

	STZ	SAZ	PFZ	AAZ
n (summer; winter)	12; 20	38; 23	31; 24	109; 18
dNi (nmol kg ⁻¹)				
Summer	3.32 \pm 0.32	3.19 \pm 0.62	4.92 \pm 0.67	6.25 \pm 0.49
Winter	2.79 \pm 0.62	3.60 \pm 0.23	5.03 \pm 0.67	6.50 \pm 0.46
PO₄ (μ mol kg ⁻¹)				
Summer	0.22 \pm 0.05	0.75 \pm 0.31	1.57 \pm 0.41	1.70 \pm 0.19
Winter	0.46 \pm 0.15	0.81 \pm 0.11	1.48 \pm 0.29	1.94 \pm 0.10
dNi: density				
Summer	0.129 \pm 0.012	0.121 \pm 0.024	0.187 \pm 0.025	0.233 \pm 0.029
Winter	0.105 \pm 0.022	0.136 \pm 0.009	0.188 \pm 0.025	0.239 \pm 0.016
Cellular Ni/P range	n.d.	n.d.	n.d.	0.2–1.4
Expected dNi uptake	n.d.	n.d.	n.d.	0.05–0.34
Measured difference	n.d.	n.d.	n.d.	0.25
% expected to measured	n.d.	n.d.	n.d.	21–136
n (summer; winter)	22; 2	8; 10	2; 4	11; 9
pNi (pmol kg ⁻¹)				
Summer	107 \pm 70	60 \pm 47	40 \pm 4	42 \pm 26
Winter	18 \pm 2	23 \pm 7	24 \pm 2	30 \pm 11
pP (nmol kg ⁻¹)				
Summer	60 \pm 27	17 \pm 14	75 \pm 7	51 \pm 19
Winter	20 \pm 6	19 \pm 6	22 \pm 4	15 \pm 4

Note. Values in bold represent significant differences between summer and winter concentrations (Wilcoxon-Mann-Whitney test; $p < 0.05$). Cellular Ni/P from Twining et al. (2013). n.d. = not determined.

concentrations. Indeed, winter phytoplankton biomass during this study was low compared to values typically observed in the Southern Ocean during summer (Weir et al., 2020). In an effort to quantify the contribution of biological uptake to the seasonal dNi cycle within the AAZ, we estimated the expected dNi (dNi_{exp}) change due to uptake only (Equation 2) and compared it to the observed dNi (dNi_{obs}) difference (Equation 3):

$$dNi_{exp} = (PO_{4win} - PO_{4sum}) \times Ni/P_{cell} \quad (2)$$

where PO_{4win} and PO_{4sum} are the average PO₄ concentrations in the mixed layer from winter and summer, respectively (Figure 3d), and Ni/P_{cell} is a range of cellular Ni to P (0.2–1.4 mmol mol⁻¹), determined from bulk particle loads representing diverse ocean settings and phytoplankton taxa (Twining et al., 2013)

$$dNi_{obs} = dNi_{win} - dNi_{sum} \quad (3)$$

where dNi_{win} and dNi_{sum} are the average measured dNi concentrations from the winter and summer mixed layers, respectively.

The results show that 21%–136% of the seasonal dNi signal in the AAZ can be accounted for by biological processes (Table 3). We can constrain this estimation by using a Ni/P_{cell} representative of Southern Ocean diatoms (0.70 \pm 0.20 mmol mol⁻¹; Twining et al., 2012) which typically dominate the AAZ (e.g., Weir et al., 2020). This leads to a 44%–78% biological component with the remainder of the dNi seasonal signal in the AAZ attributed to physical processes (e.g., deep winter mixing, lateral advection, and vertical diffusion).

The importance of biological uptake on surface dNi cycling has also been shown in several recent studies combining dNi and dNi isotope measurements from the Pacific (Bian et al., 2024; Yang et al., 2020, 2021), Atlantic (Archer et al., 2020; Lemaitre et al., 2022), and Southern Ocean (Cameron & Vance, 2014; Wang et al., 2018). A common feature emerging from these studies is the difference between Ni uptake patterns in low versus high latitude settings, that is, moderate Ni uptake (e.g., by diatoms) with negligible isotopic fractionation south of the APF and high Ni uptake (e.g., by cyanobacteria) with significant isotopic fractionation north of the APF. Using the data from this study, we calculate dNi/PO₄ and dNi/Si(OH)₄ regression slopes of 0.73 ± 0.47 and 0.018 ± 0.002 mmol mol⁻¹, respectively, for data south of the APF (<500 m, *n* = 32). North of the APF, dNi/PO₄ (1.80 ± 0.26 mmol mol⁻¹) and dNi/Si(OH)₄ (0.150 ± 0.032 mmol mol⁻¹) regression slopes for surface waters (<500 m; >20 μmol kg⁻¹ Si(OH)₄; and *n* = 44) were approximately 2.5 and 8.5 times higher, respectively. Our calculations are consistent with Archer et al., 2020 (applying the same data constraints to data from Cameron & Vance, 2014; Wang et al., 2018) and suggest that shifts in dominant phytoplankton groups across the APF, coupled with Southern Ocean surface circulation, are important processes controlling surface dNi distributions. Our calculations provide further evidence that the APF acts as biogeochemical divide for Ni, as observed for other elements (Sarmiento et al., 2004; Vance et al., 2019). These observations are also broadly consistent with trends in pNi (Figure 3b) and pNi:P ratios (Figure 3e) which increased northward across the APF, from waters generally dominated by diatoms to waters with generally higher cyanobacterial abundance. There are exceptions to these trends which further highlight the importance of phytoplankton dynamics on surface Ni cycling. First, the pNi concentrations measured north of the APF during this study remained considerably lower than comparative studies (Figure 3b). For example, pNi (18 ± 2 pmol kg⁻¹) and pNi:pP (1.12 ± 0.04 mmol mol⁻¹) that were measured in STZ waters dominated by flagellates (Weir et al., 2020) were well below the pNi (114 ± 76 pmol kg⁻¹) and pNi:pP (2.00 ± 0.76 mmol mol⁻¹) that were measured in STZ waters dominated by cyanobacteria (Wyatt et al., 2021). The greater Ni demand by cyanobacteria may stem from higher levels of Ni-SOD than other taxa (Dupont, Barbeau, & Palenik, 2008; Dupont, Neupane, et al., 2008; Twining et al., 2012). Second, winter pNi:pP ratios (1.86 ± 0.83 mmol mol⁻¹) in the AAZ were considerably higher than corresponding summer AAZ ratios (0.56 ± 0.20 mmol mol⁻¹) (Figure 3e). Here, the higher winter pNi:pP ratios were driven primarily by seasonal differences in pP concentrations (winter: 15 ± 4 pmol kg⁻¹; summer: 89 ± 44 pmol kg⁻¹), which is more likely linked to differences in phytoplankton abundance as opposed to community composition. Other notable observations include the extremely high pNi signal near Heard and McDonald Islands which suggests a strong supply of particles from freshwater input (glacial erosion and fluvial outflow) and sediment resuspension processes, as found previously for Fe (van der Merwe et al., 2019). Two high productivity SAZ stations south of Australia (Ellwood et al., 2020) had moderate to high pNi concentrations (137 ± 7 and 46 ± 7 nmol kg⁻¹; median ± sd) and high pNi:P ratios (6.5 ± 1.5 and 3.6 ± 0.4 mmol mol⁻¹; median ± sd) in the mixed layer suggesting additional Ni uptake during bloom conditions. Taken together, these observations imply that in open-ocean settings, the seasonal relationship between pNi and pNi:pP in surface waters is predominantly controlled by local phytoplankton dynamics, while in continental/margin settings, local sources driving pNi variability may be more important.

4.2. Drivers of Subsurface Ni Distributions

4.2.1. Remineralization Length Scales

Vertical attenuation factors (*b* values) for pNi and pP were calculated for full depth profiles (Table 4) from GIpr07 in order to investigate the relative remineralization length scales for these elements. For pNi, the *b* value was 0.19 ± 0.06 (mean ± sd) for the whole data set although there were significant variations between stations. Values fell between 0.11 (St 41°S) and 0.20 (St 50°S) for pNi with no clear trend. For pP, *b* values ranged between 0.27 (St 58°S) and 0.56 (St 43°S) with a value of 0.43 ± 0.10 (mean ± sd) for the whole data set. At all stations, *b* values for pNi were lower than those of pP suggesting that pNi is retained in particulate phases longer than pP, in agreement with model predictions (John et al., 2022). This is consistent with profiles of pNi:pP ratios which showed general depth increases at all stations during this study as well as in profiles from GEOTRACES transects GS01 and GIpr05 and a process study in the SAZ south of Australia (Figure 4). Exceptions to this were island-influenced stations (transect GIpr05) and two high productivity stations (IN2016-V02) where surface pNi:pP ratios were higher than in the subsurface. The differences in particle retention for these elements may be related to their physiological association with the phytoplankton cell, each with different chemical liabilities. For example, pP is associated with biomolecules such as adenosine triphosphate (ATP), deoxyribonucleic acid (DNA), and

Table 4
Vertical Attenuation Factors (*b* Values) for Particulate Phosphorus (*pP*) and Particulate Nickel (*pNi*)

Lat (°S)	Region	pP	pNi	pNi normalized to pP
41	STZ	0.42	0.11	0.26
43	SAZ	0.56	0.14	0.24
45	SAZ	0.35	0.18	0.52
48	PFZ	0.50	0.17	0.34
50	AAZ	0.45	0.20	0.44
56	AAZ	0.49	0.18	0.37
58	AAZ	0.27	0.15	0.55
All		0.43 ± 0.10	0.19 ± 0.06	0.46 ± 0.17
Boyd et al., 2017	S. Pacific	0.88 ± 0.48	0.90 ± 0.76	1.02 ± 1.01

Note. Values for all stations are mean ± sd.

ribonucleic acid (RNA) as well as phospholipid membranes, whereas Ni is associated with metalloproteins such as urease and superoxide dismutase as well as more refractory siliceous diatom frustules (Twining & Baines, 2013; Twining et al., 2012). In addition to cellular locations, further processes may preferentially enhance the vertical export of Ni over P. For example, the sorption/scavenging of dNi onto sinking particles such as manganese oxides (Fleischmann et al., 2023; Wasylenki et al., 2024) may enhance vertical Ni export compared to P. A recent study showed that two global biogeochemical ocean models (one parameterized with deeper remineralization of Ni over P and another with scavenging) reproduced field measurements accurately (John et al., 2022). Determining the relative importance of these mechanisms to Ni cycling is clearly complex and requires further investigation.

4.2.2. Estimating the Importance of Remineralized Ni

The remineralized pP component of the total measured dNi pool was calculated assuming that the O₂ deficits were solely attributed to remineralization of sinking phytoplankton cells in the subsurface water masses. When estimating remineralized dNi from O₂ deficits, the selection of the pNi:pP cellular quota is important because the elemental composition of phytoplankton is species-dependent. Using a lower and upper cellular pNi:pP estimate of 0.2 and 1.4 mmol mol⁻¹, respectively (Twining & Baines, 2013), results in a remineralized dNi component of 0.01–0.06 nmol kg⁻¹ (0%–1% of maximum measured dNi, ~8 nmol kg⁻¹) and 0.05–0.59 nmol kg⁻¹ (1%–6% of maximum measured dNi). Our calculations suggest that the locally remineralized dNi is relatively invariable (relative to total measured dNi) over a wide range of cellular quotas representing different phytoplankton species and ocean basins. Considering the upper cellular pNi:pP estimate, the maximum contribution of remineralized dNi per water mass is 4 ± 2% in AAIW, 4 ± 1% in UCDW and NADW, and 2 ± 1% in LCDW + AABW, suggesting local remineralization of sinking particles was not an important source of dNi to subsurface water masses along this transect. This is consistent with estimations from the Atlantic Ocean following a similar approach (Chen et al., 2024; Middag et al., 2020).

4.2.3. Water Mass Control on the Subsurface Distributions of dNi and Macronutrients

There was a strong correlation ($r^2 = 0.993$) between measured dNi and dNi predicted from the OMP (i.e., low residual dNi values). This means that subsurface dNi distributions can be well described without the need to invoke remineralization processes (based on oxygen deficits) occurring in the water

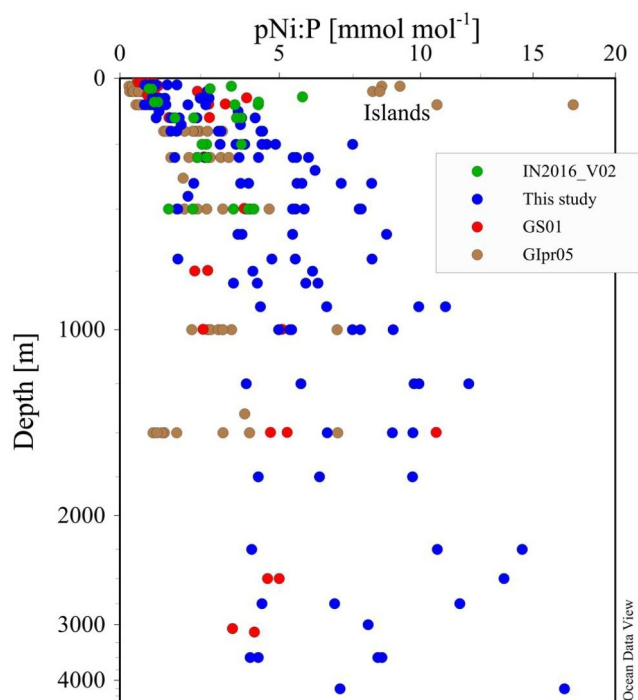


Figure 4. Vertical profiles of pNi:pP ratios from four Southern Ocean data sets, IN2016_V02 (SAZ, south of Australia), GIpr07 (this study), GS01 (Australia-Antarctica), and GIpr05 (Heard and McDonald islands). Note that the intervals on the *x*- and *y*-axes are not linear. Figure constructed using Ocean Data View (Schlitzer, 2023).

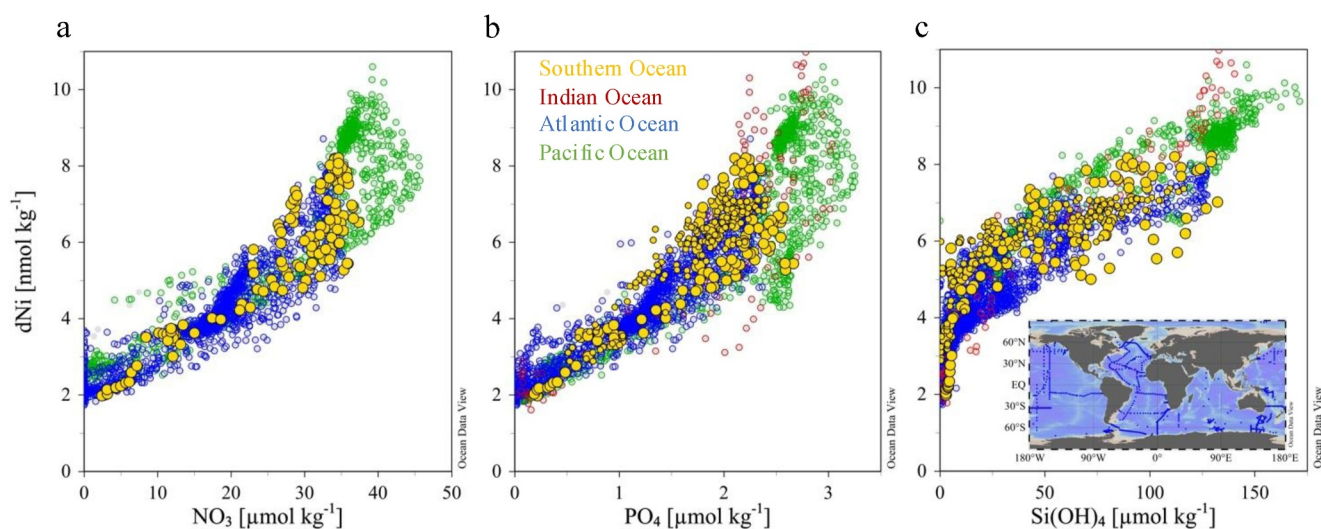


Figure 5. Scatter plots of (a) dNi versus NO_3 , (b) dNi versus PO_4 , and (c) dNi versus Si(OH)_4 for all available Southern Ocean data, including this study. These data are colored based on ocean basin. For the Southern Ocean ($<40^\circ\text{S}$), larger symbols are data from this study. Figure constructed using data from GEOTRACES IDP2021 (GEOTRACES Intermediate Data Product Group, 2021) and produced with Ocean Data View (Schlitzer, 2023).

column. As a result, subsurface dNi distributions along this section can be largely explained by physical mixing of sampled water masses. As a consequence, dNi-macronutrient relationships should also be controlled by water mass interactions, as discussed in the following section.

Using the data from this study and elsewhere in the Southern Ocean ($>40^\circ\text{S}$), we observed distinct trends in the relationships between dNi and NO_3 (Figure 5a), PO_4 (Figure 5b), and Si(OH)_4 (Figure 5c). Furthermore, when comparing the Southern Ocean data with measurements from the Atlantic, Pacific, and Indian Oceans, we observe overlapping characteristics for each of the dNi to macronutrient relationships, particularly with the Atlantic Ocean. To investigate these trends further, we assessed the ratio of dNi to macronutrients (dNi: NO_3 , dNi: PO_4 , and dNi: Si(OH)_4) per water mass, with a focus on comparing Southern Ocean and Atlantic derived water masses. Note that the spot ratio described here (dNi:macronutrient) is different from regression slopes (dNi/macronutrient) because all dNi to macronutrient regression slopes have positive y intercepts, that is, there is always ‘left over’ dNi when macronutrient concentrations are at, or near, zero.

For dNi: NO_3 (Figure 6a) and dNi: PO_4 (Figure 6b), the ratios showed more subtle variations between the water masses compared to dNi: Si(OH)_4 (Figure 6c), which decreased approximately threefold between AAIW and deep waters (NADW and LCDW + AABW). Furthermore, the dNi: NO_3 and dNi: PO_4 ratios in the source region for NADW (0.23 ± 0.01 and $3.40 \pm 10 \text{ mmol mol}^{-1}$, respectively; Figure S6 in Supporting Information S1) were on average slightly higher than for the Antarctic origin water masses it mixes with during southward advection across the equator. In contrast, the dNi: Si(OH)_4 ratio in the source region for NADW (0.37 ± 0.03 ; Figure S6 in Supporting Information S1) was far greater than the Antarctic origin water masses. This suggests that the dNi, NO_3 , and PO_4 content of NADW is modified by mixing to a lesser extent than Si(OH)_4 which increases significantly southward, primarily through mixing with bottom waters with Si(OH)_4 maxima (Middag et al., 2020). When removing the remineralized dNi component, ratios of preformed dNi to macronutrients (dNi_{preformed}:macronutrient) do not vary significantly from ratios of dNi:macronutrient (Figure S7 in Supporting Information S1). The preformed dNi component explained 96%, 97%, 96%, and 98% of dNi distributions (and therefore dNi to macronutrient ratios), in AAIW, UCDW, NADW, and LCDW + AABW, respectively. Thus, while subsurface dNi distributions and dNi:macronutrient relationships are driven by mixing of water masses with different end-member compositions, there is an increased importance for biological processes in surface waters. As described earlier (Section 4.1), there is a distinct difference between upper water column dNi versus PO_4 (and NO_3) and dNi versus Si(OH)_4 relationships on either side of the APF. South of the APF, these relationships are consistent with the uptake characteristics of diatoms. The subsequent northward advection of surface waters with moderately depleted dNi, PO_4 , and NO_3 and heavily depleted Si(OH)_4 (Middag et al., 2020; Vance et al., 2019) create nutrient conditions favoring different phytoplankton groups and ultimately results in a

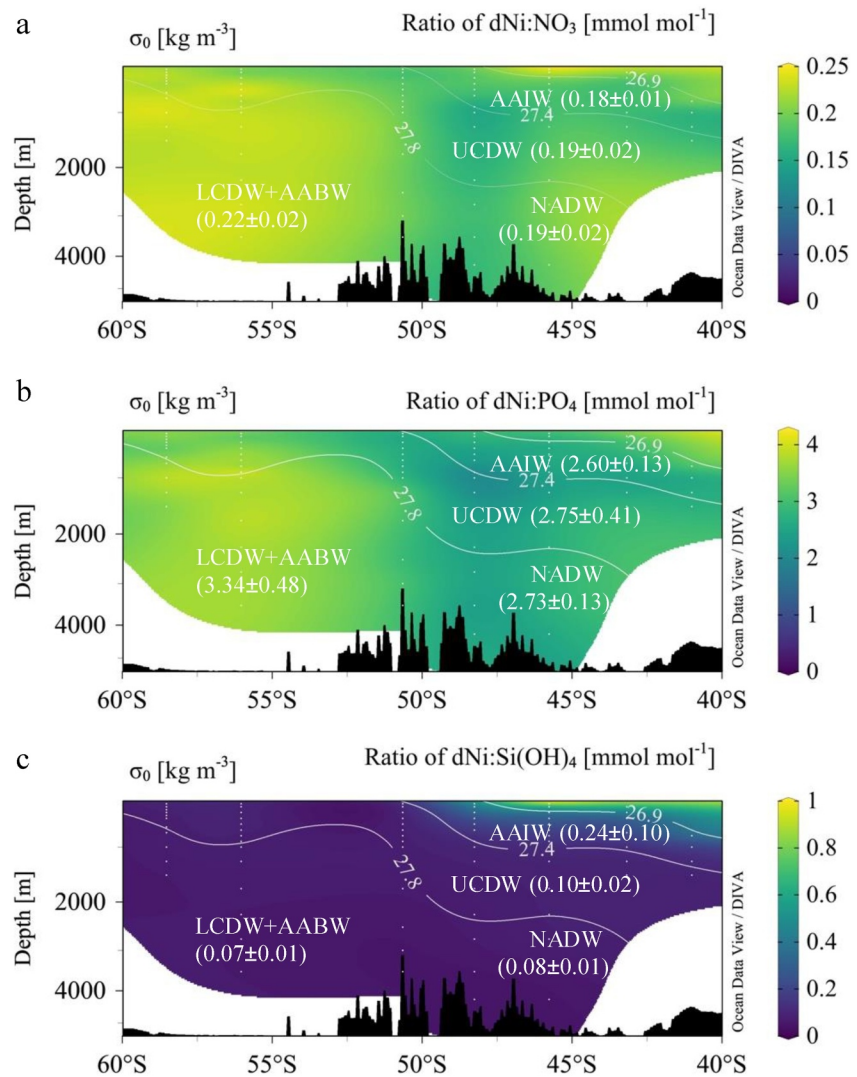


Figure 6. Sections of key subsurface water masses in the Southern Ocean showing ratios (mean \pm sd) of dNi to (a) NO_3 , (b) PO_4 , and (c) Si(OH)_4 . Isolines represent potential densities (σ_0) aimed at delineating water mass depths. Water mass abbreviations as per Figure 2. Figure constructed with Ocean Data View (Schlitzer, 2023).

greater change in the gradient of dNi to Si(OH)_4 concentrations across the APF than dNi to PO_4 and NO_3 concentrations (Figure 5, Figure S8 in Supporting Information S1). Combining these surface and subsurface observations, we find that the dNi to macronutrient relationships cannot be described by a single universal regression and, instead, are composed of multiple regressions that are determined by a combination of surface ocean biogeochemistry and water mass end-member mixing. Compared to relationships of dNi: NO_3 and PO_4 , the dNi: Si(OH)_4 relationship shows more pronounced trends at low versus high concentrations owing to the unique uptake characteristics of diatoms at high latitudes, surface circulation, and higher end-member variability of Antarctic versus Atlantic derived water masses. Our findings agree with Ni data from the Atlantic Ocean (Chen et al., 2024; Middag et al., 2020) and elsewhere in the Southern Ocean (Janssen et al., 2020) and reinforce the common theme that biological and physical coupling in the Southern Ocean are largely responsible for setting oceanic nutrient distributions (De Souza & Morrison, 2024; Sarmiento et al., 2004).

5. Conclusion

The first winter measurements of dissolved Ni (dNi) and particulate Ni (pNi) from the Indian sector of the Southern Ocean are presented. These data provide new insights regarding the seasonal cycling of Ni as well as the

processes governing dissolved-particulate exchange and dNi-macronutrient cycling. Using a comprehensive Ni compilation sourced from the GEOTRACES IDP2021, we show that differences in dNi concentrations within the winter and summer surface mixed layer north of the Antarctic Polar Front were not significant and were driven by physical mixing processes. South of the Antarctic Polar Front, the seasonal dNi signal was significant owing to a combination of physical mixing and increased seasonal variation in biological uptake. However, the seasonal dNi cycle is sensitive to temporal shifts in phytoplankton community composition and abundance. Using calculated vertical attenuation factors and an optimum multiparameter analysis, we show that pNi is retained in the particulate phase longer than for pP, and that dNi sourced through remineralization of particle-associated pNi is small with respect to dNi present within subsurface water masses in the Southern Ocean. While biologically driven processes are important in surface waters, subsurface distributions of dNi and dNi to macronutrient relationships in the Southern Ocean are primarily driven by water mass end-member mixing as observed in other basins for example, the Atlantic (Chen et al., 2024; Middag et al., 2020). By greatly expanding winter dNi and pNi observations in the Southern Ocean, this study helps to constrain the balance between biological and physical drivers of the Ni seasonal cycle in the source region for globally important water masses.

Data Availability Statement

Dissolved and particulate nickel data and CTD and macronutrient data as well as the outputs of the OMP water mass analysis are available in an open access repository (Cloete et al., 2024). Nickel data used in the seasonal Southern Ocean compilation are publicly available through the GEOTRACES Intermediate Data Product 2021 (GEOTRACES Intermediate Data Product Group, 2021).

Acknowledgments

We would like to thank the South African National Antarctic Programme (SANAP) as well as Captain Knowledge Bengu and the crew of the R/V SA Agulhas II for their professionalism and support during the winter 2017 voyage. We acknowledge Chief Scientist Marcello Vichi and all the participants involved in the expedition. We are grateful to the “TracEx” team for their help in collecting trace-clean seawater samples, and to Shantelle Smith, Raquel Flynn, Raymond Roman, Kurt Spence, and Sarah Fawcett (University of Cape Town) for use of macronutrient data. The GEOTRACES 2021 Intermediate Data Product (IDP2021 V2) represents an international collaboration and is endorsed by the Scientific Committee on Oceanic Research (SCOR). The many researchers and funding agencies responsible for the collection of data and quality control are thanked for their contributions to the IDP2021, in particular, Michael Ellwood, Yoshiki Sohrin, Linjie Zheng, Edward Butler, Corey Archer, Derek Vance, Thomas Holmes, Melanie Gault-Ringold, Pauline Latour, Kathrin Wuttig, Christina Schallenberg, Angela Milne, and Maeve Lohan for allowing unpublished data to be included in this manuscript. Ryan Cloete was supported through the National Research Foundation (NRF) Innovation PhD studentship and a postdoctoral bursary from Whales and Climate Change program. He is now supported through funding from the European Union’s Horizon 2020 research and innovation program under the Marie Skłodowska-Curie grant agreement No 899546 during his postdoc at LEMAR. This research was supported by NRF grants (UID# 93069, 105826 and 110715) and funds from the Whales and Climate Change program to A. R. S.F. acknowledges funding from NRF (UID# 111210, 110731).

References

- Anderson, L. A., & Sarmiento, J. L. (1994). Redfield ratios of remineralization determined by nutrient data analysis. *Global Biogeochemical Cycles*, 8(1), 65–80. <https://doi.org/10.1029/93GB03318>
- Anderson, R. F. (2020). Geotraces: Accelerating research on the marine biogeochemical cycles of trace elements and their isotopes. *Annual Review of Marine Science*, 12(1), 49–85. <https://doi.org/10.1146/annurev-marine-010318>
- Archer, C., Vance, D., Milne, A., & Lohan, M. C. (2020). The oceanic biogeochemistry of nickel and its isotopes: New data from the South Atlantic and the Southern Ocean biogeochemical divide. *Earth and Planetary Science Letters*, 535, 116118. <https://doi.org/10.1016/j.epsl.2020.116118>
- Bian, X., Yang, S. C., Raad, R. J., Odendahl, C. E., Lanning, N. T., Sieber, M., et al. (2024). Distribution and cycling of nickel and nickel isotopes in the Pacific Ocean. *Geophysical Research Letters*, 51(16). <https://doi.org/10.1029/2024GL111115>
- Boyd, P. W., Ellwood, M. J., Tagliabue, A., & Twining, B. S. (2017). Biotic and abiotic retention, recycling and remineralization of metals in the ocean. *Nature Geoscience*, 10(3), 167–173. <https://doi.org/10.1038/ngeo2876>
- Cameron, V., & Vance, D. (2014). Heavy nickel isotope compositions in rivers and the oceans. *Geochimica et Cosmochimica Acta*, 128, 195–211. <https://doi.org/10.1016/j.gca.2013.12.007>
- Castrillejo, M., Statham, P. J., Fones, G. R., Planquette, H., Idrus, F., & Roberts, K. (2013). Dissolved trace metals (Ni, Zn, Co, Cd, Pb, Al, and Mn) around the Crozet islands, Southern Ocean. *Journal of Geophysical Research: Oceans*, 118(10), 5188–5201. <https://doi.org/10.1002/jgrc.20359>
- Chen, X. G., Gledhill, M., Lohan, M. C., Milne, A., & Achterberg, E. P. (2024). Surface ocean biogeochemistry and deep ocean circulation control relationships between nutrient-type trace metals (Cd, Ni, Cu, and Zn) and nutrients in the South Atlantic Ocean near the subtropical front. *Geochimica et Cosmochimica Acta*, 370, 144–160. <https://doi.org/10.1016/j.gca.2024.01.001>
- Cloete, R., Loock, J. C., Mtshali, T., Fietz, S., & Roychoudhury, A. N. (2019). Winter and summer distributions of Copper, zinc and nickel along the international GEOTRACES section GIPY05: Insights into deep winter mixing. *Chemical Geology*, 511, 342–357. <https://doi.org/10.1016/j.chemgeo.2018.10.023>
- Cloete, R., Loock, J. C., van Horsten, N., Chen, X.-G., Planquette, H., & Roychoudhury, A. N. (2024). Winter dissolved and particulate nickel concentrations along 30 deg E transect, Southern Ocean: GEOTRACES GIPr07 cruise (version V2). *Zenodo*. [Dataset]. <https://doi.org/10.5281/zenodo.14039790>
- Cloete, R., Loock, J. C., van Horsten, N. R., Fietz, S., Mtshali, T. N., Planquette, H., & Roychoudhury, A. N. (2021). Winter biogeochemical cycling of dissolved and particulate cadmium in the Indian sector of the Southern Ocean (GEOTRACES GIPr07 transect). *Frontiers in Marine Science*, 8. <https://doi.org/10.3389/fmars.2021.656321>
- Cutter, G., Casciotti, K., Croot, P., Geibert, W., Heimbürger, L.-E., Lohan, M., et al. (2017). Sampling and sample-handling protocols for GEOTRACES cruises. <https://www.geotraces.org/methods-cookbook/>
- Cuvelier, M. L., Allen, A. E., Monier, A., McCrow, J. P., Messié, M., Tringe, S. G., et al. (2010). Targeted metagenomics and ecology of globally important uncultured eukaryotic phytoplankton. *Proceedings of the National Academy of Sciences of the United States of America*, 107(33), 14679–14684. <https://doi.org/10.1073/pnas.1001665107>
- De Souza, G., & Morrison, A. K. (2024). The Southern Ocean hub for nutrients, micronutrients, and their isotopes in the global ocean. *Oceanography*, 37(2). <https://doi.org/10.5670/oceanog.2024.414>
- Dupont, C. L., Barbeau, K., & Palenik, B. (2008). Ni uptake and limitation in marine Synechococcus strains. *Applied and Environmental Microbiology*, 74(1), 23–31. <https://doi.org/10.1128/AEM.01007-07>
- Dupont, C. L., Neupane, K., Shearer, J., & Palenik, B. (2008). Diversity, function and evolution of genes coding for putative Ni-containing superoxide dismutases. *Environmental Microbiology*, 10(7), 1831–1843. <https://doi.org/10.1111/j.1462-2920.2008.01604.x>
- Ellwood, M. J. (2008). Wintertime trace metal (Zn, Cu, Ni, Cd, Pb and Co) and nutrient distributions in the Subantarctic Zone between 40–52°S; 155–160°E. *Marine Chemistry*, 112(1–2), 107–117. <https://doi.org/10.1016/j.marchem.2008.07.008>

- Ellwood, M. J., Strzpek, R., Chen, X., Trull, T. W., & Boyd, P. W. (2020). Some observations on the biogeochemical cycling of zinc in the Australian sector of the Southern Ocean: A dedication to Keith Hunter. *Marine and Freshwater Research*, 71(3), 355–373. <https://doi.org/10.1071/MF19200>
- Evans, N., Schroeder, I. D., Pozo Buil, M., Jacox, M. G., & Bograd, S. J. (2020). Drivers of subsurface deoxygenation in the southern California current system. *Geophysical Research Letters*, 47(21). <https://doi.org/10.1029/2020GL089274>
- Fleischmann, S., Du, J., Chatterjee, A., McManus, J., Iyer, S. D., Amonkar, A., & Vance, D. (2023). The nickel output to abyssal pelagic manganese oxides: A balanced elemental and isotope budget for the oceans. *Earth and Planetary Science Letters*, 619, 118301. <https://doi.org/10.1016/j.epsl.2023.118301>
- GEOTRACES Intermediate Data Product Group (2021). The GEOTRACES intermediate data product 2021 version 2 (IDP2021v2). *NERC EDS British Oceanographic Data Centre NOC*.
- Grun, R., Samanta, M., & Ellwood, M. J. (2023). Variability in zinc:phosphorous and zinc:silicon ratios and zinc isotope fractionation in Southern Ocean diatoms: Observations from laboratory and field experiments. *Marine Chemistry*, 257, 104330. <https://doi.org/10.1016/j.marchem.2023.104330>
- Janssen, D. J., Sieber, M., Ellwood, M. J., Conway, T. M., Barrett, P. M., Chen, X., et al. (2020). Trace metal and nutrient dynamics across broad biogeochemical gradients in the Indian and Pacific sectors of the Southern Ocean. *Marine Chemistry*, 221, 103773. <https://doi.org/10.1016/j.marchem.2020.103773>
- John, S. G., Kelly, R. L., Bian, X., Fu, F., Smith, M. I., Lanning, N. T., et al. (2022). The biogeochemical balance of oceanic nickel cycling. *Nature Geoscience*, 15(11), 906–912. <https://doi.org/10.1038/s41561-022-01045-7>
- John, S. G., Liang, H., Pasquier, B., Holzer, M., & Silva, S. (2024). Biogeochemical fluxes of nickel in the global oceans inferred from a diagnostic model. *Global Biogeochemical Cycles*, 38(5). <https://doi.org/10.1029/2023GB008018>
- Karstensen, J., & Tomczak, M. (1998). Age determination of mixed water masses using CFC and oxygen data. *Journal of Geophysical Research*, 103(C9), 18599–18609. <https://doi.org/10.1029/98JC00889>
- Lam, P. J., & Marchal, O. (2015). Insights into particle cycling from thorium and particle data. *Annual Review of Marine Science*, 7(1), 159–184. <https://doi.org/10.1146/annurev-marine-010814-015623>
- Lemaitre, N., Du, J., de Souza, G. F., Archer, C., & Vance, D. (2022). The essential bioactive role of nickel in the oceans: Evidence from nickel isotopes. *Earth and Planetary Science Letters*, 584, 117513. <https://doi.org/10.1016/j.epsl.2022.117513>
- Li, H. T., Tuo, S. H., Lu, M. C., & Ho, T. Y. (2022). The effects of Ni availability on H₂ production and N₂ fixation in a model unicellular diazotroph: The expression of hydrogenase and nitrogenase. *Limnology & Oceanography*, 67(7), 1566–1576. <https://doi.org/10.1002/lno.12151>
- Martin, J. H., Knauer, G. A., David, ~, Karl, M., & Broenkow, W. W. (1987). Vertex: Carbon cycling in the northeast pacific. *Deep-Sea Research*, 34(2), 267–285. [https://doi.org/10.1016/0198-0149\(87\)90086-0](https://doi.org/10.1016/0198-0149(87)90086-0)
- Middag, R., de Baar, H. J. W., Bruland, K. W., & van Heuven, S. M. A. C. (2020). The distribution of nickel in the west-Atlantic ocean, its relationship with phosphate and a comparison to cadmium and zinc. *Frontiers in Marine Science*, 7(105). <https://doi.org/10.3389/fmars.2020.00105>
- Orsi, A. H., Whitworth, T., & Nowlin, W. D. (1995). On the meridional extent and fronts of the Antarctic Circumpolar Current. *Deep Sea Research Part I: Oceanographic Research Papers*, 42(5), 641–673. [https://doi.org/10.1016/0967-0637\(95\)00021-W](https://doi.org/10.1016/0967-0637(95)00021-W)
- Peers, G. S., Milligan, A. J., & Harrison, P. J. (2000). Assay optimization and regulation of urease activity in two marine diatoms. *Journal of Phycology*, 36(3), 523–528. <https://doi.org/10.1046/j.1529-8817.2000.99037.x>
- Planquette, H., & Sherrell, R. M. (2012). Sampling for particulate trace element determination using water sampling bottles: Methodology and comparison to in situ pumps. *Limnology and Oceanography: Methods*, 10(5), 367–388. <https://doi.org/10.4319/lom.2012.10.367>
- Pollard, R. T., Lucas, M. I., & Read, J. F. (2002). Physical controls on biogeochemical zonation in the Southern Ocean. *Deep-Sea Research II*, 49(16), 3289–3305. [https://doi.org/10.1016/S0967-0645\(02\)00084-X](https://doi.org/10.1016/S0967-0645(02)00084-X)
- Ragsdale, S. W. (2009). Nickel-based enzyme systems. *Journal of Biological Chemistry*, 284(28), 18571–18575. <https://doi.org/10.1074/jbc.R900020200>
- Samanta, S., Cloete, R., Loock, J., Rossouw, R., & Roychoudhury, A. N. (2021). Determination of trace metal (Mn, Fe, Ni, Cu, Zn, Co, Cd and Pb) concentrations in seawater using single quadrupole ICP-MS: A comparison between offline and online preconcentration setups. *Minerals*, 11, 1289. <https://doi.org/10.3390/min11111289>
- Sarmiento, J. L., Gruber, N., Brzezinski, M. A., & Dunne, J. P. (2004). High-latitude controls of thermocline nutrients and low latitude biological productivity. *Nature*, 427(6969), 56–60. <https://doi.org/10.1038/nature02204>
- Schlitzer, R. (2023). *Ocean Data View*. odv.awi.de.
- Sclater, F. R., Boyle, E., & Edmond, J. M. (1976). On the marine geochemistry of nickel. *Earth and Planetary Science Letters*, 31(1), 119–128. [https://doi.org/10.1016/0012-821X\(76\)90103-5](https://doi.org/10.1016/0012-821X(76)90103-5)
- Swart, S., Speich, S., Ansoorge, I. J., & Lutjeharms, J. R. E. (2010). An altimetry-based gravest empirical mode south of Africa: 1. Development and validation. *Journal of Geophysical Research*, 115(3). <https://doi.org/10.1029/2009JC005299>
- Tagliabue, A., Sallée, J. B., Bowie, A. R., Lévy, M., Swart, S., & Boyd, P. W. (2014). Surface-water iron supplies in the Southern Ocean sustained by deep winter mixing. *Nature Geoscience*, 7(4), 314–320. <https://doi.org/10.1038/ngeo2101>
- Talley, L. D., Pickard, G. L., William, E. J., & Swift, J. H. (2011). *Descriptive physical Oceanography: An introduction*. Academic Press.
- Tomczak, M., & Large, D. G. B. (1989). Optimum multiparameter analysis of mixing in the thermocline of the eastern Indian Ocean. *Journal of Geophysical Research*, 94(C11), 16141–16149. <https://doi.org/10.1029/jc094ic11p16141>
- Traill, C. D., Conde-Pardo, P., Rohr, T., van der Merwe, P., Townsend, A. T., Latour, P., et al. (2024). Mechanistic constraints on the drivers of Southern Ocean Meridional iron distributions between Tasmania and Antarctica. *Global Biogeochemical Cycles*, 38(3). <https://doi.org/10.1029/2023GB007856>
- Twining, B. S., & Baines, S. B. (2013). The trace metal composition of marine phytoplankton. *Annual Review of Marine Science*, 5(1), 191–215. <https://doi.org/10.1146/annurev-marine-121211-172322>
- Twining, B. S., Baines, S. B., Vogt, S., & Nelson, D. M. (2012). Role of diatoms in nickel biogeochemistry in the ocean. *Global Biogeochemical Cycles*, 26(4). <https://doi.org/10.1029/2011GB004233>
- Vance, D., Little, S. H., De Souza, G. F., Khatiwala, S., Lohan, M. C., & Middag, R. (2017). Silicon and zinc biogeochemical cycles coupled through the Southern Ocean. *Nature Geoscience*, 10(3), 202–206. <https://doi.org/10.1038/ngeo2890>
- van der Merwe, P., Wuttig, K., Holmes, T., Trull, T. W., Chase, Z., Townsend, A. T., et al. (2019). High lability Fe particles sourced from glacial erosion can meet previously unaccounted biological demand: Heard Island, Southern Ocean. *Frontiers in Marine Science*, 6. <https://doi.org/10.3389/fmars.2019.00332>

- Van Horsten, N. R., Planquette, H., Sarthou, G., Ryan-Keogh, T. J., Lemaitre, N., Mtshali, T. N., et al. (2022). Early winter barium excess in the southern Indian Ocean as an annual remineralisation proxy (GEOTRACES GIPr07 cruise). *Biogeosciences*, *19*(13), 3209–3224. <https://doi.org/10.5194/bg-19-3209-2022>
- Wang, R. M., Archer, C., Bowie, A. R., & Vance, D. (2019). Zinc and nickel isotopes in seawater from the Indian Sector of the Southern Ocean: The impact of natural iron fertilization versus Southern Ocean hydrography and biogeochemistry. *Chemical Geology*, *511*, 452–464. <https://doi.org/10.1016/j.chemgeo.2018.09.010>
- Wasylenki, L. E., Wells, R. M., Spivak-Birndorf, L. J., Baransky, E. J., & Frierdich, A. J. (2024). Toward mending the marine mass balance model for nickel: Experimentally determined isotope fractionation during Ni sorption to birnessite. *Geochimica et Cosmochimica Acta*, *379*, 76–88. <https://doi.org/10.1016/j.gca.2024.06.022>
- Weir, I., Fawcett, S., Smith, S., Walker, D., Bornman, T., & Fietz, S. (2020). Winter biogenic silica and diatom distributions in the Indian sector of the Southern Ocean. *Deep-Sea Research Part I Oceanographic Research Papers*, *166*, 103421. <https://doi.org/10.1016/j.dsr.2020.103421>
- Wyatt, N. J., Milne, A., Achterberg, E. P., Browning, T. J., Bouman, H. A., Woodward, E. M. S., & Lohan, M. C. (2021). Seasonal cycling of zinc and cobalt in the south-eastern Atlantic along the GEOTRACES GA10 section. *Biogeosciences*, *18*(14), 4265–4280. <https://doi.org/10.5194/bg-18-4265-2021>
- Yang, S. C., Hawco, N. J., Pinedo-González, P., Bian, X., Huang, K. F., Zhang, R., & John, S. G. (2020). A new purification method for Ni and Cu stable isotopes in seawater provides evidence for widespread Ni isotope fractionation by phytoplankton in the North Pacific. *Chemical Geology*, *547*, 119662. <https://doi.org/10.1016/j.chemgeo.2020.119662>
- Yang, S. C., Kelly, R. L., Bian, X., Conway, T. M., Huang, K. F., Ho, T. Y., et al. (2021). Lack of redox cycling for nickel in the water column of the Eastern tropical north pacific oxygen deficient zone: Insight from dissolved and particulate nickel isotopes. *Geochimica et Cosmochimica Acta*, *309*, 235–250. <https://doi.org/10.1016/j.gca.2021.07.004>

References From the Supporting Information

- Pardo, P. C., Pérez, F. F., Velo, A., & Gilcoto, M. (2012). Water masses distribution in the Southern Ocean: Improvement of an extended OMP (eOMP) analysis. *Progress in Oceanography*, *103*, 92–105. <https://doi.org/10.1016/j.pocean.2012.06.002>
- Rudnick, R. L., & Gao, S. (2003). Composition of the continental crust. *Treatise on Geochemistry*, 3–9, 1–64. <https://doi.org/10.1016/B978-0-08-095975-7.00301-6>
- Talley, L. D. (2013). Hydrographic atlas of the world ocean circulation experiment (WOCE). In M. Sparrow, P. Chapman, & J. Gould (Eds.), *Volume 4: Indian Ocean*. International WOCE Project Office. ISBN 0904175588.